Modeling the frequency response of an acoustic cavity using the method of images

Frank Rice[a)]
California Institute of Technology, 103-33, Pasadena, California 91125

Teresa Riedel[b)]
Ball Aerospace & Technologies Corporation, Boulder, Colorado 80301

Isaiah Curtis[c)]
California Institute of Technology, MSC 230, Pasadena, California 91126

(Received 5 September 2022; accepted 29 December 2022)

We demonstrate the ability of a simple algorithm based on the venerable method of images (MOIs), to accurately model the detailed frequency response of a multidimensional, rectangular, lossy resonant cavity. The convergence properties of the model's infinite series solution are shown to be determined by the cavity's quality factor Q. A 1D example demonstrates that the MOI series converges to the exact solution. Next, a comparison to precisely measure 2D cavity data confirms that a straightforward extension of the 1D algorithm to multiple dimensions provides accurate results. The algorithm is short, easily understandable by undergraduate students and relatively undemanding to code. An example using ®MATHEMATICA is provided.
https://doi.org/10.1119/5.0124415

I. INTRODUCTION

Midway through their sophomore year, our physics majors are introduced to the rigors and the joys of experimental science by a required and quite difficult lab course. Having just completed a one-term lecture course introducing the analyses of oscillations, waves, and normal modes (albeit mostly in one dimension), they now learn how to collect and analyze frequency and energy spectra generated by a variety of phenomena. These experiences during lab provide students with a useful working knowledge of several subjects later covered in detail by upper division lecture courses.

One of the lab course's more popular experiments involves the determination of the dispersion relation of sound waves in air by observing and analyzing the normal mode frequencies of a small acoustic cavity. Figure 1 is a photo of the apparatus, and Fig. 2 shows a high-resolution measurement of the cavity's frequency response. The expected normal mode wave numbers are calculated from the rectangular cavity's measured dimensions, and these are matched with the corresponding peaks in its measured frequency response. The rectangular cavity has thick acrylic side walls and a thinner top surface. Its bottom surface is provided by the sturdy aluminum base plate upon which it rests. The source sound transducer (speaker) is mounted in a side wall near the cavity's bottom right corner in the photo. The response transducer (microphone) is mounted beneath the center of the base plate. (The small opening for this transducer is visible in the base plate just to the left of center of the cavity's upper side wall.) Moving the cavity around on the base plate changes the relative position of the response transducer within it.

The data plotted in Fig. 2 consist of (response transducer)/(source transducer) signal voltage amplitude ratios (gains) measured at 2070 frequencies with the transducers positioned near diagonally opposite corners of the cavity. As expected, the frequency response peaks correspond to the cavity's normal modes. If air is nondispersive, then these frequencies should be proportional to the cavity's normal mode wave numbers. A proportional, least-squares fit of the observed peaks' frequencies to their corresponding normal mode wave numbers (calculated from the measured cavity dimensions, assuming that the cavity is rectangular) was performed by optimizing its slope, i.e., the average phase velocity of sound in air over the measured frequency range. The fit result was quite consistent with the hypothesis that air is nondispersive over this frequency range. The dashed vertical lines in Fig. 2 show predicted cavity resonant frequencies calculated from the mode wave numbers and the best fit slope.[1]

The accuracy and large dynamic range of the experiment's data acquisition system enable it to provide a wealth of details in the measured gain and phase responses of the cavity. It should come as no surprise that the cavity's frequency response peaks at nearly every normal mode, because, given

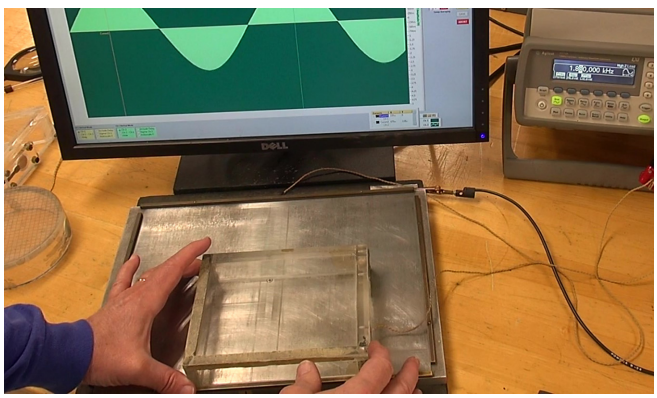

Fig. 1. Configuration of the experimental apparatus. The interior of the rectangular acrylic box is approximately 152 mm × 114 mm × 32 mm. The metal plate serves as the cavity's bottom boundary, and the small hole at the plate's center marks the position of the sound pressure response transducer (a microphone). Its amplified signal is displayed on the computer monitor as the experimenter moves the box around on the base plate, mapping out the mode's nodal line structure. The selected normal mode corresponds the cavity's third resonance, near 1.9 kHz.

its construction, the quality factor Q of the cavity's resonances should be on the order of 100. What might be surprising, on the other hand, is the rich structure evident in the response at intermediate frequencies. Interestingly, between several pairs of resonant frequencies, the response drops sharply by as much as two orders of magnitude, a seemingly resonant-like behavior for which the transducer positions correspond to nodes rather than antinodes. Between other peaks, however, the response gently falls and rises. This variation in behavior piques the interest of many of our more sophisticated students as well as our TAs, and we devote the remainder of this text to model the driven response of the cavity as a function of frequency.

II. STEADY-STATE RESPONSE OF A 1D CAVITY

As a warm-up exercise, first consider a familiar, one-dimensional example: A resonant cavity consisting of a section of electromagnetic transmission line of length L with reflective terminations at positions $x=0$ and $x=L$. Assume that the line is linear, homogeneous, and nondispersive, but it has a finite quality factor Q. The cavity is driven by a constant-amplitude, sinusoidal source coincident with the termination at $x=0$.

A. Exact solution

This 1D system is simple enough to solve exactly. Once the system reaches steady state, the transmission line supports two traveling waves moving in opposite directions with a common wave number k. Let $V_+(x)$ be the complex-valued *voltage amplitude phasor* of the wave traveling toward larger x values, and $V_-(x)$ that of the wave traveling in the opposite direction.[2] With both waves present, the total voltage phasor $V(x)$ at some position x on the line will then equal $V_+(x)+V_-(x)$. Assume the line terminations to be ideal, free boundaries for a wave's voltage (i.e., the boundaries have infinite impedances), so that at a termination, the reflected wave's phasor will equal that of the incident wave.

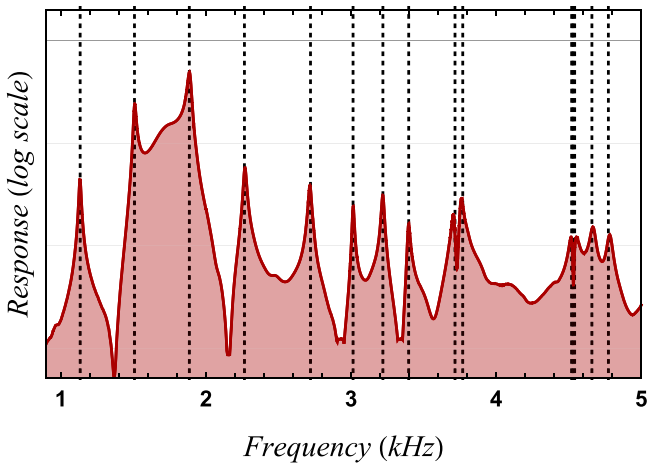

Fig. 2. Measured frequency response of the cavity. The curve shows the actual data (no smoothing applied). The logarithmic vertical scale has grid lines separated by factors of 10. The measured response is generally higher for frequencies of 1.4–2.1 kHz, because the conversion efficiencies of the two transducers are highest in that range. The dashed vertical lines show the expected set of resonant frequencies determined by the slope of a linear fit of the observed response peaks vs the cavity's expected normal mode wave numbers calculated from its measured dimensions.

At the right-hand boundary $x=L$, it must then be the case that $V_-(L)=V_+(L)$. At the $x=0$ termination, the outgoing wave $V_+(0)$ must also include the driving source power. Denote the complex-valued source amplitude phasor as V_S, so that $V_+(0)=V_-(0)+V_S$. This model provides a *wave representation* of the state of the system,[3] presenting us with an *inhomogeneous boundary value problem* because of the presence of V_S.

The waves V_+ and V_- propagate on the transmission line in their respective directions. If the line were not lossy, then the complex phasors representing these traveling waves would have constant magnitudes as their phases change with position: $V_+(x+d)=V_+(x)\exp(ikd)$ and $V_-(x+d)=V_-(x)\exp(-ikd)$. Loss introduces a decrease in amplitude along the direction of propagation that will generally be frequency dependent and, thus, also dependent on the wave number k. We specify this loss using the quality factor $Q(k)$, where the wave's squared amplitude (proportional to its intensity) decreases as it propagates, e-folding with the *attenuation length* $\lambda(k)=Q(k)/k$. Including this attenuation with distance, the two waves' *propagation operators*, or *propagators*, $\mathcal{P}_+$ and $\mathcal{P}_-$, become

$$V_+(x+d)=\mathcal{P}_+(d)\,V_+(x) \text{ and } V_-(x+d)=\mathcal{P}_-(d)\,V_-(x), \tag{1}$$

where

$$\mathcal{P}_+(d)=\exp\left[ikd\left(1+\frac{i}{2Q}\right)\right] \text{ and } \mathcal{P}_-(d)=\exp\left[-ikd\left(1+\frac{i}{2Q}\right)\right]. \tag{2}$$

We use the propagators $\mathcal{P}_+$ and $\mathcal{P}_-$ to tidy up our derivations. Note a couple of their properties: $\mathcal{P}_-(d)=\mathcal{P}_+(-d)=1/\mathcal{P}_+(d)$ and $\mathcal{P}_+(d_1+d_2)=\mathcal{P}_+(d_1)\,\mathcal{P}_+(d_2)$. The loss factor is parameterized by $Q(k)$ rather than $\lambda(k)$. For many systems, it turns out that $Q(k)$ is a more slowly varying function of k than is $\lambda(k)$, except near a resonant absorption feature. The forms in Eq. (1) for $V_+(x)$ and $V_-(x)$ provide the traveling wave components we use to derive the solution to the boundary value problem. This solution will yield $V(x)$, the complex-valued voltage phasor field on the transmission line in terms of the source excitation's amplitude V_S and its frequency (actually wave number k)

$$V(x)=V_+(x)+V_-(x)=\mathcal{P}_+(x)\,V_+(0)+\mathcal{P}_-(x)\,V_-(0). \tag{3}$$

Express $V_-(0)$ in terms of $V_+(0)$ using the boundary condition at $x=L$

$$\begin{aligned} V_-(0)&=\mathcal{P}_-(-L)\,V_-(L)=\mathcal{P}_-(-L)\,V_+(L)\\ &=\mathcal{P}_-(-L)\,\mathcal{P}_+(L)\,V_+(0)=\mathcal{P}_+(2L)\,V_+(0),\\ \text{so that}\quad \mathcal{P}_-(x)\,V_-(0)&=\mathcal{P}_-(x)\,\mathcal{P}_+(2L)\,V_+(0)\\ &=\mathcal{P}_+(2L-x)\,V_+(0). \end{aligned} \tag{4}$$

Next, express $V_+(0)$ in terms of V_S,

$$V_S=V_+(0)-V_-(0)=V_+(0)[1-\mathcal{P}_+(2L)],$$
$$\therefore\quad V_+(0)=V_S\left[\frac{1}{1-\mathcal{P}_+(2L)}\right]. \tag{5}$$

Finally, put these expressions together to derive the 1D cavity's complex-valued response function, $H(k,x) \equiv V(x)/V_S$,

$$\begin{aligned} V(x) &= V_+(x) + V_-(x) = [\mathcal{P}_+(x) + \mathcal{P}_+(2L-x)]V_+(0) \\ &= \left[\frac{\mathcal{P}_+(x) + \mathcal{P}_+(2L-x)}{1-\mathcal{P}_+(2L)}\right] V_S, \quad \text{and} \\ H(k,x) &= \frac{\mathcal{P}_+(x) + \mathcal{P}_+(2L-x)}{1-\mathcal{P}_+(2L)} \\ &= \frac{\mathcal{P}_+(x-L) + \mathcal{P}_+(L-x)}{\mathcal{P}_+(-L) - \mathcal{P}_+(L)}. \end{aligned} \tag{6}$$

The final expression for H in Eq. (6) was obtained by multiplying the previous one by $\mathcal{P}_+(-L)/\mathcal{P}_+(-L)$ and distributing through its numerator and denominator. The dependence of H on x and L is explicit in these expressions; its dependence on k and Q is through the propagator definitions in Eq. (2). The final form for H in Eq. (6) is straightforward to convert to an equivalent trigonometric expression

$$H(k,x) = i\,\frac{\cos[k(L-x)(1+i/2Q)]}{\sin[kL(1+i/2Q)]}. \tag{7}$$

For reasonably high Q, the denominator will be small for $k_n = n\pi/L$ and positive integer n. At $x = L$, $|H(n\pi/L, L)| = 1/\sinh(n\pi/2Q) \approx (2/\pi)(Q/n)$ for large Q/n. Clearly, the k_n denote the cavity's resonant wave numbers, and the $H(k_n, x)$ approach ideal normal modes as $Q \to \infty$.

B. Method of images model

Now we derive a *method of images* (MOIs) approach that leads to a result equivalent to Eq. (6) for the 1D cavity's response function. Consider again the first equality in that expression

$$H(k,x) = \frac{\mathcal{P}_+(x) + \mathcal{P}_+(2L-x)}{1-\mathcal{P}_+(2L)}.$$

Now expand the division by $(1-\mathcal{P}_+(2L))$, creating an equivalent series expression. Recalling that $[\mathcal{P}_+(2L)]^m = \mathcal{P}_+(2mL)$, the expression becomes

$$\begin{aligned} H(k,x) = {} & [\mathcal{P}_+(x) + \mathcal{P}_+(2L-x)] \\ & \times [1 + \mathcal{P}_+(2L) + \mathcal{P}_+(4L) + \mathcal{P}_+(6L) + \cdots], \end{aligned} \tag{8}$$

$$\begin{aligned} H(k,x) = {} & \mathcal{P}_+(x) \quad \langle \text{direct path contribution from the source} \rangle \\ & + \mathcal{P}_+(x)\,[\mathcal{P}_+(2L) + \mathcal{P}_+(4L) + \mathcal{P}_+(6L) + \cdots] \\ & \langle \text{left images} \rangle \\ & + \mathcal{P}_+(-x)\,[\mathcal{P}_+(2L) + \mathcal{P}_+(4L) + \mathcal{P}_+(6L) + \cdots] \\ & \langle \text{right images} \rangle. \end{aligned} \tag{9}$$

Equation (8) is an infinite series representation of the exact solution, Eq. (6). It is also the series that would result by adding the signals from an infinite array of identical sources arranged along an infinite transmission line, the sources spaced at intervals of $2L$, and the sum of their individual voltage phasor contributions measured at a point located a distance $x \le L$ from the nearest source. This infinite series for H converges absolutely for finite Q and $k > 0$. The ratio of the magnitudes of successive series terms is $\exp(-kL/Q)$, which will approach 1 if $kL \ll Q$. In this case, the required number of series terms for an accurate model calculation may be large, as illustrated in Fig. 3.

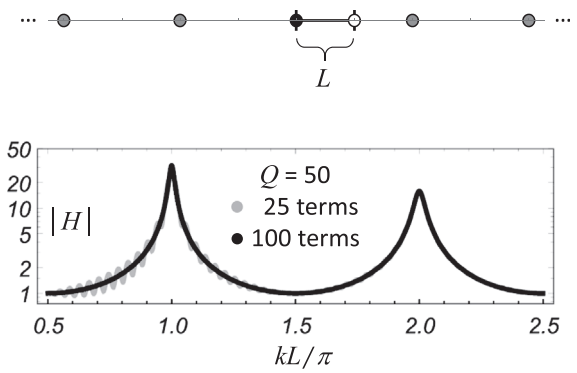

Fig. 3. MOI model of the 1D cavity. The top graphic shows the configuration of the source V_S (black circle), the sense position at the opposite termination $V(x = L)$ (white circle), and image sources (gray circles) spaced at intervals of $2L$. The bottom graphic shows the model frequency response results for $Q = 50$. The black curve is for 100 terms of the Eq. (8) series (equivalent to 200 image sources) and the gray curve is for 25 terms (50 image sources). The plot shows the two lowest resonances, where convergence is slowest. The 100-term calculation has a maximum relative error of 0.5% (at $kL/\pi = 0.745$).

Keeping the series solution in mind, reconsider the original 1D cavity configuration: the terminations at 0 and L, the source coincident with the termination at 0, and the measurement point at position x, $0 \le x \le L$. Now think of the measured signal $V(x) = V_+(x) + V_-(x)$ constructed as follows: the signal from the source reaches x with relative amplitude $\mathcal{P}_+(x)$. This signal continues onward and reflects from the termination at L to return through x with relative amplitude $\mathcal{P}_-(x-L)\,\mathcal{P}_+(L) = \mathcal{P}_+(-x)\,\mathcal{P}_+(2L)$, adding this value to the measurement. The signal then reflects again at 0 (now with relative amplitude $\mathcal{P}_+(2L)$), subsequently passing yet again by x with $\mathcal{P}_+(x)\,\mathcal{P}_+(2L)$, and so on. The total signal measured at x is the sum of these contributions, leading again to the series solution in Eq. (8). Thus, the members of the infinite array of sources described in the preceding paragraph represent the source along with an infinite sequence of its mirror images, reflected by the terminations. Equation (9) rearranges the series representation of $H(k, x)$ as a sum of signals from the real source and this sequence of reflections. This idea will be the basis of the method of images algorithm presented in Sec. III.

III. MODELING THE MULTIDIMENSIONAL CAVITY

The method used in Sec. II to calculate an exact solution to the steady-state response of a 1D resonator is very difficult to extend to the multidimensional geometry of the acoustic cavity shown in Fig. 1. Useful alternative approaches typically generate an infinite series, which is then truncated to provide adequate accuracy in an approximate method. One approach, especially when dealing with a high-Q system, might be to perform some form of normal mode expansion of the inhomogeneous part of the boundary value problem, generating a set of coupling coefficients to the homogeneous system's eigenfunctions. Typical examples might include the coupling of free-space signals into an antenna or optical

system and estimating the changes to resonator's normal modes induced by a small perturbing effect on its state or geometry. Another common practice, especially in commercial software used to model very complicated structures, is to discretize the system boundaries and volume and employ one of a variety of techniques such as finite element, finite difference, and the method of moments approaches.[4]

Presented here is a quite different and simple approach that is easy to understand, even by early undergraduates: we extend the MOI model from Sec. II to the acoustic cavity's multidimensional geometry and use it to numerically approximate the cavity's detailed frequency response for any choice of positions for the source and detector within it.[5] The model can be adapted to accommodate mixed boundary conditions, boundaries that are not perfectly reflective, and transducers that are not isotropic. The method is, unfortunately, limited to only a small set of cavity geometries. Fortunately, a rectangular geometry happens to be a member of this set. The Appendix provides a brief derivation of the boundary value problem for the complex-valued sound wave pressure phasor field $p(\mathbf{r})$ induced in our acoustic cavity and calculates the cavity's normal modes. It also shows that the physical dimensions of the cavity (Fig. 1) effectively reduce the required model geometry to only two dimensions, but extending the analysis to three dimensions is straightforward. This exercise is an example of finding a *Green's function* solution to the problem.[6]

A. Image source lattice construction

The reflection of an isotropic source wave from a flat cavity boundary can be modeled as an identical wave emitted by an image source as shown in Fig. 4. The advantage of this model is immediately apparent: The image's location is unaffected by the detector location or any other model parameter such as k or Q. One, therefore, need only calculate the distance to the detector from the image in order to determine the reflected wave's contribution to the response phasor at the detector's location. It is relatively straightforward to include not only the attenuations introduced by the propagating medium but also to add factors to the image phasor that incorporate any additional amplitude and phase effects introduced by the reflection at the boundary.[7]

The rectangular cavity's multiple boundaries and consequent multiple wave reflections complicate the situation. Each of the four planar boundaries, of course, requires the inclusion of its own mirror image of the source. Waves from

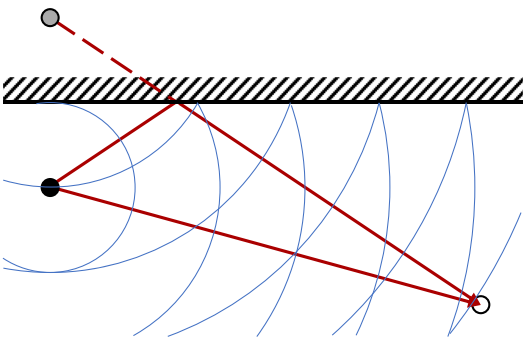

Fig. 4. Source and its image from a planar surface. The source (black circle) and its mirror image (gray) radiate identical waves. The signal phasor at the detector (white circle) is the coherent sum of these two signals. The arcs show corresponding surfaces of equal phase for the two emissions.

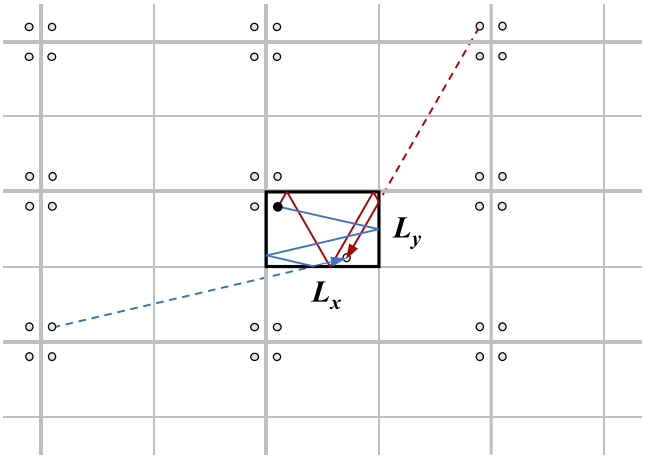

Fig. 5. A lattice of cavity images. The original, rectangular cavity and its enclosed source (black boundary and disk) have mirror images tiling the plane. The pattern repeats at intervals of $2L_x$ horizontally and $2L_y$ vertically. Also shown are examples of how a ray to the detector from each image source corresponds to a unique reflected signal path within the cavity from the real source.

these images, however, will reflect from the other interior surfaces of the cavity, and those subsequent reflections must be accounted for. Thus, each image requires the inclusion of more images to account for these reflected waves, and so on. The result is an infinite lattice of image sources whose phasor contributions become the terms in our series solution for the cavity's response.

Constructing the lattice of image sources is conceptually simple: reflect the geometry of the cavity (including the source) across each of its boundaries and then reflect each of these images across its own boundaries, etc., until the entire plane (or 3D space) is tiled with cavity images. The sources within these images then constitute the infinite set of image sources to be used in the series solution. Figure 5 illustrates a possible result of this process. In this example, the actual signal source is located at an interior point of the rectangular cavity. Note how the source images form identical clusters, regularly spaced at intervals of twice the horizontal and vertical cavity dimensions, a generalization of the 1D image pattern shown in Fig. 3.

As with the 1D example, each image source corresponds to a unique, reflected path from the real source to detector within the cavity. This correspondence is illustrated by two example paths in Fig. 5. Note how the lengths and angles of the reflected path segments correspond to segments of the direct path from the image to detector as that path passes through intervening cavity images. The countably infinite number of reflected paths from the source to detector make up a set isomorphic with the set of image source positions, and the lengths of two corresponding paths match. These are the essential properties that allow the MOI series expansion to succeed.[8]

B. Propagators and the calculation algorithm

Now consider the driven acoustic cavity, whose state, as shown in the Appendix, may be described by a scalar pressure field p. We continue to assume that the driving source radiates isotropically into the cavity interior, and the wave medium is homogeneous, linear, and isotropic. Given these characteristics, we may conclude that the pressure field

associated with the emitted wave from any source in the image lattice can be characterized by a complex-valued pressure phasor whose value at any location depends only on its distance r from the source: $p = p(r)$. Because the isotropic natures of source and medium ensure that the wave's local wave vector $\mathbf{k}$ is parallel to the location's radius vector $\mathbf{r}$ from the source, the phase of $p(r)$ is determined by a simple, scalar calculation: $\exp(i\,\mathbf{k}\cdot\mathbf{r}) = \exp(ikr)$.

The amplitude of an emitted wave's phasor depends on two factors. First is a geometric factor which requires that, in the absence of absorption by the medium or the cavity boundaries, the net total power escaping from an imaginary surface containing the source must be independent of the surface's size and shape. For the effectively 2D cavity geometry, this factor must, therefore, be $r^{-1/2}$. Second comes the loss of power in the emitted wave. Air at ordinary lab temperatures and pressures offers very little attenuation to acoustic waves at audio frequencies. Attenuation in the apparatus shown in Fig. 1 is dominated by acoustic radiation escaping from the cavity and by frictional losses, both mainly caused by sound-induced vibrations of the acrylic box and base plate forming the cavity. Nevertheless, we assume that this attenuation may be adequately described by a quality factor $Q(k)$ attributed to the medium (air), just as for the 1D example presented earlier. The amplitude attenuation factor is then $\exp[-kr/(2Q)]$, cf. Eq. (2). This is, of course, a greatly simplified model of the actual loss processes. The final expression for a source's pressure field phasor becomes

$$p(r) = r^{-1/2}\,\exp(ikr)\,\exp[-kr/(2Q)], \tag{10}$$

where r is the distance from the source and Q will be a function of the wave number k.[9] The contribution of the nth image source, located at $\mathbf{r}_n$, to the total response phasor field value at the detector position $\mathbf{r}_d$ is calculated using $r_n = |\mathbf{r}_n - \mathbf{r}_d|$ in Eq. (10). The image source contributions coherently add to generate the field value $p(\mathbf{r}_d)$,

$$p(\mathbf{r}_d) = \sum_{n=1}^{\infty} \frac{\exp(ikr_n)}{\sqrt{r_n}}\,\exp\left[-\frac{kr_n}{2Q}\right]. \tag{11}$$

C. Convergence and accuracy of the model calculations

Consider the convergence of the infinite series of image contributions to the field value $p(\mathbf{r}_d)$ given in Eq. (11). Let L_x be the long dimension of the cavity, and let $R \gg L_x$ be some very large distance. As $R \to \infty$, the number of image sources N for which $|R - r_n| < L_x$ grows proportionally to R: $N \approx (2\pi R)(2L_x)/(L_xL_y) \sim 4\pi R/L_y$. If there is no loss, then as $R \to \infty$ these sources' contribution to $p(\mathbf{r}_d)$ will be

$$\left|\sum^{N} \frac{\exp(ikr_n)}{\sqrt{r_n}}\right| \approx \frac{\left|\sum^{N} \exp(ikr_n)\right|}{\sqrt{R}}. \tag{12}$$

However, the sum in the numerator is just that of N unit vectors in the complex plane with uncorrelated directions (phases), so as N becomes large $|\Sigma \exp(ikr_n)| \to \sqrt{N} \sim 2\sqrt{\pi R/L_y}$. Therefore, as $R \to \infty$, Eq. (12) approaches a constant, and, if the system is lossless, the ratio test for absolute convergence fails.[10] As was the case for the 1D example, the series convergence is dependent on the loss factor $\exp[-kr_n/(2Q)]$, and an approximate expression for the magnitude of the total contribution of these N image sources to $p(\mathbf{r}_d)$ is

$$\left|\sum^{N} \frac{\exp(ikr_n)}{\sqrt{r_n}}\,\exp\left[-\frac{kr_n}{2Q}\right]\right| \sim 2\sqrt{\frac{\pi}{L_y}}\exp\left[-\frac{kR}{2Q}\right]. \tag{13}$$

Again taking L_x to be the cavity's long dimension, consider a sequence of circles centered on the detector position $\mathbf{r}_d$ with radii $R_m = (2m-1)L_x$ for positive integers m. These circles then define a set of annuli with outer and inner radii of $R_m \pm L_x$, which tile the plane. The set of lattice sources within each annulus generates a contribution to the response phasor $p(\mathbf{r}_d)$ given in Eq. (11). The magnitude of this contribution may be estimated using $R = (2m-1)L_x$ in Eq. (13), an estimate which will be quite accurate for $m \gg 1$. Now assume that we truncate the infinite series for $p(\mathbf{r}_d)$, including only those sources within the annuli defined by $1 \le m \le m_0$ for some $m_0 \gg 1$. We wish to estimate the accuracy of this approximation of the infinite series by estimating the relative magnitude of the sum of the contributions of the excluded sources.

For the longest wavelength mode, $k = \pi/L_x$; for a given Q, this value of k will yield a slower convergence than for higher-order modes. Using this value, consider the annulus defined by $R_m = (2m-1)L_x$. Let C_m equal the magnitude of the total contribution from sources in this annulus estimated using Eq. (13)

$$\begin{aligned} C_m &\sim 2\sqrt{\frac{\pi}{L_y}}\exp\left[-\frac{\pi R_m}{2QL_x}\right] = 2\sqrt{\frac{\pi}{L_y}}\exp\left[-\frac{\pi(2m-1)}{2Q}\right] \\ &= \left[2\sqrt{\frac{\pi}{L_y}}\exp\left(\frac{\pi}{2Q}\right)\right]\exp\left(-\frac{\pi}{Q}\right)^{m}. \end{aligned} \tag{14}$$

The C_m are approximated by terms of an infinite geometric series that converges if $Q > 0$. Designate the sum of these terms from m to ∞ as S_m. Then

$$\begin{aligned} S_m &= \left[2\sqrt{\frac{\pi}{L_y}}\exp\left(\frac{\pi}{2Q}\right)\right]\sum_{j=m}^{\infty}\exp\left(-\frac{\pi}{Q}\right)^{j} \\ &= \left[2\sqrt{\frac{\pi}{L_y}}\exp\left(\frac{\pi}{2Q}\right)\right]\exp\left(-\frac{\pi}{Q}\right)^{m} \\ &\quad\times\left[1-\exp\left(-\frac{\pi}{Q}\right)\right]^{-1}. \end{aligned} \tag{15}$$

Assume that the full series S_1 will give a rough approximation of the magnitude of the detector's response $p(\mathbf{r}_d)$ for the lowest mode $k = \pi/L_x$ and with quality factor Q. An estimate of the fractional error introduced by the truncation of the MOI model infinite series for $p(\mathbf{r}_d)$ at the annulus defined by $R_{m_0} = (2m_0 - 1)L_x$ is then S_{m_0+1}/S_1,

$$\begin{aligned} \text{fractional error} &\sim S_{m_0+1}/S_1 \\ &= \exp\left(-\frac{\pi}{Q}\right)^{m_0+1}\exp\left(-\frac{\pi}{Q}\right)^{-1} \\ &= \exp\left(-\frac{\pi}{Q}\right)^{m_0} = \exp\left(-\frac{m_0\pi}{Q}\right). \end{aligned} \tag{16}$$

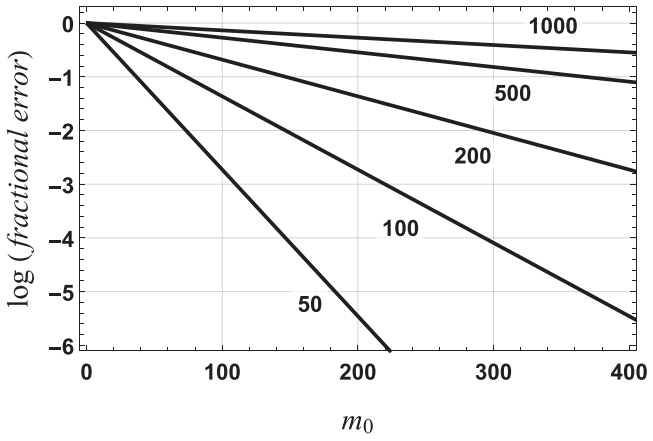

Fig. 6. Estimated relative errors vs m_0 and Q. Shown are several plots of the Eq. (16) fractional error estimate as a function of the index m_0 at which the infinite series for $p(\mathbf{r}_d)$ is truncated. Each line is labeled with the cavity Q value used to generate it. The logarithms are base 10.

It must be emphasized that, given the several approximations used to develop Eq. (16), this expression for the fractional error in the MOI method provides only an order-of-magnitude estimate. Nevertheless, it is a useful tool for setting the values of computational parameters used in an MOI algorithm. These results are for $k = \pi/L_x$, the lowest frequency resonant mode of the cavity, for which the series convergence is slowest.

Figure 6 provides a graphical analysis of the relative error estimate Eq. (16) in terms of the series truncation index m_0 and cavity Q. This analysis applies to the lowest resonant mode of the cavity. For a higher frequency resonance, divide the model cavity Q by the ratio of the desired frequency to that of its the lowest mode before consulting Fig. 6. The plots clearly demonstrate that the MOI approach can result in a very inefficient model of a high-Q cavity, but it places much more reasonable computational demands when modeling cavities with Qs of less than a couple of hundred.

IV. MODEL IMPLEMENTATION, RESULTS, AND DISCUSSION

Section III provided the details of an infinite series solution for the steady-state frequency response of a rectangular acoustic cavity such as that shown in Fig. 1. The series solution was developed using a method of images approach that is particularly well suited to systems of moderate quality factor Q. We now use the results of the last section to assess the computational demands required to accurately model the frequency response of the cavity shown in Fig. 1, whose measured response was presented in Fig. 2. The widths of the resonance peaks in that figure indicate that the cavity's Q is approximately 80–150. Knowing that the errors plotted in Fig. 6 are order-of-magnitude estimates, and because we wish our model to accurately capture the details of the response between the resonance peaks, we will make conservative use of that figure's estimates: For $Q = 150$ and an error target of 0.1%, Fig. 6 suggests that an appropriate truncation limit would be $m_0 \approx 300$. With $L_y/L_x = 3/4$, the interior of a circle with radius $2m_0L_x = 600L_x$ will include approximately 1.5×10^6 image sources. The calculation of $p(\mathbf{r}_d)$ using Eq. (11) requires a distance calculation followed by an exponential and two trigonometric function calls for each of these sources. This computational effort yields a calculation of the response at a single location in the cavity for a single wave number, k. Clearly, careful choice of programming environment and algorithm organization will be important. A ®MATHEMATICA notebook with a reasonably efficient algorithm is available online.[11]

Our implementation of the MOI model was configured to approximate the conditions of the measured frequency response dataset of Fig. 2. It used the measured cavity dimensions and the speed of sound determined from that data.[1] To simplify image source indexing for the model calculations, a square area with side lengths of $2 \times 600L_x$ was chosen rather than a circular area of radius $600L_x$. This increased the number of images to over 1.9×10^6. To ease this potential computational burden, the modeled source position was selected to be a corner of the cavity, collapsing each cluster of four image sources (Fig. 5) to a single source and reducing the number of sources to just over 481 000. A further simplification was to choose $\mathbf{r}_d$ as the diagonally opposite corner. This placed the images symmetrically around the response location, reducing the number of unique $p(r)$ calculations from 1.9×10^6 to only approximately 121000 per frequency (or k).

Comparisons of the measured data to a calculation using this MOI model are shown in Figs. 7 and 8. In order to approximate the behavior of the measured data peak widths vs frequency, the $Q(f)$ function used for the model increased linearly from $Q(1.1\text{kHz}) = 80$ to $Q(4.5\text{kHz}) = 220$. This observed $Q(f)$ behavior may be due to a reduced ability of the sound to excite vibrations of the cavity's acrylic box at higher frequencies, reducing the level of vibration-induced sound emissions. The model took 158 s of the CPU time to calculate responses at the 2403 frequencies plotted in Fig. 7, equivalent to approximately 1.8×10^6 $p(r)$ calculations per second (or about 15 frequencies per second).

The relatively simple, straightforward MOI model algorithm was, nevertheless, able to capture the rich structure of the acoustic cavity response with detail that is quite similar to that of the measured data, even given its assumption of a 2D model, the chosen source and detector positions, and

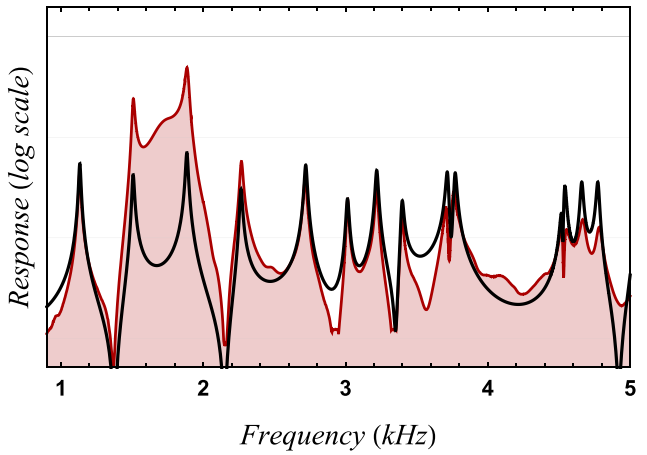

Fig. 7. Comparison of the model to measured data. The model source position $\mathbf{r}_s$ was in a corner of the cavity, and the detector position $\mathbf{r}_d$ was chosen to be the diagonally opposite corner. Approximately 121 000 complex-valued response calculations were performed for each of 2403 frequencies. The result was normalized to match the measured data near 3 kHz.

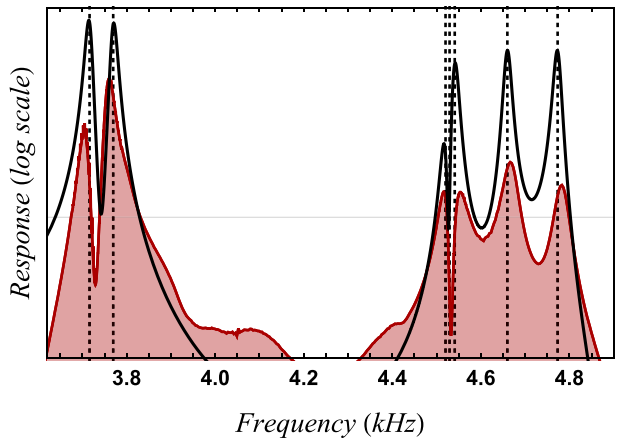

Fig. 8. Detail of the model vs measured data. The model successfully reproduces the sharp dips in the response in these clusters of resonances. Also shown are the positions of the ideal normal mode frequencies as indicated in Fig. 2. The complicated frequency response structure around these nearly degenerate modes (especially the triplet at 4.53 kHz) is addressed in Sec. 3 of the Appendix.

very simple loss model. On the other hand, its fidelity to the measured data leaves much to be desired. The primary flaw is its omission of the frequency responses of the transducers used to generate and detect the sound. The two transducers were identical, quite old hearing aid speakers, a vintage of the late 1960s. The reciprocal nature of these purely electromechanical devices allows one to serve as a detector microphone while its twin serves as the source speaker. Their frequency response is limited for a variety of reasons, the primary one being that they were designed to optimize a hearing-impaired user's ability to understand the spoken word. As mentioned previously, they have an enhanced response over a small range of frequencies centered at 1.7 kHz. Their small size and design cause their response at lower frequencies to fall rapidly, whereas their high frequency response falls more gradually to provide some ambient noise filtering.

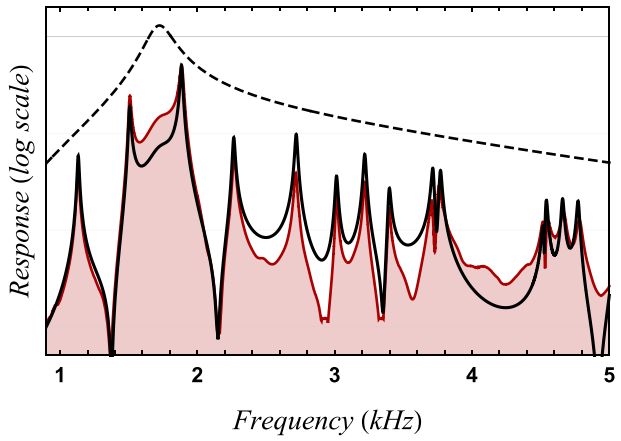

Fig. 9. Applying a transducer frequency response model. The upper dashed curve shows the transducer frequency response model used to correct the MOI results. It is meant to model the combined effects of both transducers, and it peaks at 1.72 kHz with a Q of 9. The corrected MOI model was calculated by multiplying the complex-valued MOI and transducer response phasors at each frequency.

A simple filter model was created to approximate the observed transducer frequency response effects on the measured data. This model was applied to the MOI result, and the filter parameters were adjusted to optimize the match between the simulation and the measurements. The improved model result is presented in Fig. 9. The remaining discrepancies in its fidelity to the measured data are probably due mainly to its simplistic loss model: Eq. (10) with a linear model for $Q(f)$.

In conclusion, the method of images approach can clearly be quite successful at calculating the steady-state frequency responses of resonant cavities with simple geometries and moderate quality factors. Although not nearly so capable or as fast as the sophisticated algorithms used by commercial software, it has its own advantages. In particular, a program to efficiently implement an MOI algorithm consists of only a couple of dozen lines of code. As such, the algorithm is well-suited for instruction, especially for undergraduates at the junior or even sophomore level.

AUTHOR DECLARATIONS

Conflict of Interest

The authors have no conflicts to disclose.

APPENDIX: SUPPLEMENTAL INFORMATION

1. Wave equation for sound propagation

Assume that the sound wave medium (air in this case) is an isotropic, homogeneous, ideal fluid (continuous, linear, zero viscosity, and lossless) with equilibrium pressure p_0 and density ρ_0, which at sea level are approximately 1.01×10^5 pascal and 1.23 g/l, respectively. Given these assumptions, a sound wave induces a stress tensor field on the medium that reduces to the combination of a scalar pressure change $p(\mathbf{r},t)$ and its gradient vector $\nabla p(\mathbf{r},t)$. Furthermore, assume that sound waves will disturb the equilibrium values by very small amounts, i.e., $p(\mathbf{r},t) \ll p_0$.[12]

A tiny parcel of air within the cavity at equilibrium position $\mathbf{r}$ responds to the sound in two ways: (1) $\rho(\mathbf{r},t)$, its change in density away from ρ_0, varies adiabatically with the local pressure change $p(\mathbf{r},t)$; and (2) its center of mass is accelerated by the local pressure gradient $\nabla p(\mathbf{r},t)$. The first effect defines a velocity, which turns out to be the speed of sound, c_s,

$$c_s^2 = (\partial p/\partial \rho)|_{p_0,\rho_0} = p(\mathbf{r},t)/\rho(\mathbf{r},t) = \Gamma p_0/\rho_0. \tag{A1}$$

For small, adiabatic pressure oscillations at audio frequencies, the ratio of specific heats Γ of dry air at room temperature is very close to the ideal diatomic gas value of 1.4. At ultrasonic frequencies, CO_2 plays a larger role in determining dry air's Γ, and air becomes slightly dispersive.[13]

The vector displacement field $\mathbf{X}(\mathbf{r},t)$ of the air parcels' positions away from equilibrium is influenced by both effects

$$\text{acceleration: } \nabla p(\mathbf{r},t) = -\rho_0 \frac{\partial^2 \mathbf{X}(\mathbf{r},t)}{\partial t^2}, \tag{A2}$$

$$\text{continuity: } \nabla \cdot \mathbf{X}(\mathbf{r},t) = -\frac{\rho(\mathbf{r},t)}{\rho_0}. \tag{A3}$$

Combining these three equations results in a homogeneous wave equation for the time-varying sound pressure amplitude field $p(\mathbf{r},t)$,

$$\begin{aligned}\text{from (A2): } \nabla^2 p(\mathbf{r},t) &= -\rho_0 \nabla \cdot \frac{\partial^2 \mathbf{X}(\mathbf{r},t)}{\partial t^2} \\ &= -\rho_0 \frac{\partial^2}{\partial t^2} \nabla \cdot \mathbf{X}(\mathbf{r},t), \\ \text{from (A3) and (A1):} &= \frac{\partial^2 \rho(\mathbf{r},t)}{\partial t^2} = c_s^{-2} \frac{\partial^2 p(\mathbf{r},t)}{\partial t^2}. \end{aligned} \quad \text{(A4)}$$

For a sinusoidal wave oscillating at angular frequency ω, $p(\mathbf{r},t) = \mathrm{Re}\,[p(\mathbf{r})\exp(-i\omega t)]$, defining the wave's complex-valued pressure phasor field $p(\mathbf{r})$. Substituting this expression for $p(\mathbf{r},t)$ into Eq. (A4) results in the phasor field's corresponding Helmholtz equation

$$\nabla^2 p(\mathbf{r}) + k^2 p(\mathbf{r}) = 0, \quad \text{where} \quad k \equiv \omega/c_s. \quad \text{(A5)}$$

Clearly, k is the wave number, thus showing that c_s, defined in Eq. (A1), is the sound wave's phase velocity v_ϕ.

2. Boundary conditions and normal modes

If the cavity walls are rigid, then their shapes and positions are unaffected by the sound pressure field within the cavity, and a tiny air parcel abutting a wall is unable to move in a direction perpendicular to it. Therefore, at a rigid boundary with surface normal $\mathbf{n}(\mathbf{r})$, it must be the case that $\mathbf{n}(\mathbf{r}) \cdot \partial^2 \mathbf{X}(\mathbf{r},t)/\partial t^2 = 0$, implying that

$$\mathbf{n}(\mathbf{r}) \cdot \nabla p(\mathbf{r}) = 0. \quad \text{(A6)}$$

The rigid cavity walls are, therefore, free boundaries for the sound pressure field, and Eqs. (A5) and (A6) define the Neumann boundary value problem for the sound pressure phasor field.[14]

Equations (A5) and (A6) separate in a Cartesian coordinate system, and, because the cavity is rectangular, this is an obvious choice. Aligning the origin and the axes with a cavity corner and its adjoining three edges almost makes the solution obvious by inspection. Assign L_x, L_y, and L_z as the three cavity edge lengths, and assume a formal solution of $p(\mathbf{r}) = p_x(x)p_y(y)p_z(z)$. The separated differential equations become

$$\begin{aligned} &p_x''(x) + k_x^2 p_x(x) = 0 \quad \text{with} \\ &p_x'(0) = p_x'(L_x) = 0 \quad (\text{ditto for } y \text{ and } z), \end{aligned} \quad \text{(A7)}$$

with the solution, for nonnegative integers l, m, and n such that $l + m + n > 0$

$$k_l = \pi l/L_x, \quad k_m = \pi m/L_y, \quad k_n = \pi n/L_z, \quad \text{(A8)}$$

$$k_{l,m,n}^2 = k_l^2 + k_m^2 + k_n^2, \quad \text{(A9)}$$

$$\text{and} \quad p_{l,m,n}(x,y,z) = \cos(k_l x)\cos(k_m y)\cos(k_n z). \quad \text{(A10)}$$

The pressure field phasor $p(\mathbf{r}) = p_{l,m,n}(x,y,z)$ in Eq. (A10) has been assigned a phase that makes it a real number. The three cosine factors have identical phases (real). In terms of traveling waves, each cosine term can be written as a sum of oppositely directed traveling waves, e.g., $\cos(k_l x) = (1/2)(e^{ik_l x} + e^{-ik_l x})$. Multiplying these expressions and gathering terms will show that $p_{l,m,n}(x,y,z)$ can be written as a sum of as many as eight equal-amplitude plane waves, all with wave vectors whose squared magnitudes equal $k_{l,m,n}^2$, Eq. (A9), and whose vector sum vanishes.

The original, homogeneous boundary value problem for these free oscillations, Eqs. (A5) and (A6), is, of course, an eigensystem problem. The $k_{l,m,n}^2$ are the eigenvalues and the $p_{l,m,n}(x,y,z)$ their corresponding eigenfunctions. Because the problem's differential equations, both for the cavity interior and for its boundaries, do not include damping or loss terms, the eigenvalues are all real. The solutions constitute the set of ideal cavity normal modes, a complete set of orthogonal basis states for sound waves in an ideal, rectangular cavity.

The longest side of the cavity was designed to have length $L_x = 6.00$ in. or 15.24 cm. The other two side lengths were designed to be $L_y = 4.50$ in. and $L_z = 1.25$ in.. The measured lengths are 15.225, 11.442, and 3.185 cm. The measured L_x and L_y values are each within 0.1% of their design values, and their ratio is 0.2% away from the designed 4 : 3 value. The L_z value is about 0.3% greater than its design length. These numbers set the relevant wave number and, therefore, frequency ranges of the experiment. The lowest frequency mode will have wave number $k_{1,0,0} = \pi/L_x$ with a wavelength equal to $2L_x$. Taking the speed of sound to be 344.7 m/s,[1] the lowest mode frequency is expected to be 1.132 kHz. (The measured frequency was 1.1323 kHz.)

The lowest mode frequency with a z-component variation corresponds to $k_{0,0,1}$, which is L_x/L_z times that of the lowest mode. The location of the driving source, however, has $z = L_z/2$ (see Fig. 1). However, this lowest z-mode has a nodal surface at $L_z/2$, as shown in Eq. (A10). This implies that the source position makes it impossible for the source to excite this mode. The lowest excitable mode for this configuration must be $k_{0,0,2}$ with frequency $2L_x/L_z$ times the lowest mode frequency of 1.132 or 10.8 kHz.

This lowest frequency involving a mode with a z component to its wave vector, 10.8 kHz, exceeds the high frequency response limit of the transducers. Thus, the wave vectors relevant to the experiment will all have vertical index $n = 0$, effectively reducing the cavity geometry to only two dimensions for the behavior of the pressure field $p(\mathbf{r},t)$ generated by the driving source and its images, and even with the detector transducer located in the bottom surface of the cavity ($z = 0$), its signal is representative of the cavity pressure field at any z, except, perhaps, when located very near the driving source transducer. Consequently, we will refer to only the x and y components of the cavity wave vectors with their associated mode indices l and m.

3. Behavior at degenerate mode frequencies

The rectangular cavity's normal mode eigenfunctions $p_{l,m}(x,y)$ have a particularly simple structure (note that the z component factor has been removed from Eq. (A10) because it $\equiv 1$ and is, thus, irrelevant at the frequencies we consider). If either the x or y cosine factor's argument in Eq. (A10) is an odd multiple of $\pi/2$, then $p_{l,m}(x,y) = 0$. This criterion defines the function's nodal lines, and in this case, the nodal lines are straight and aligned with the cavity boundaries. The mode index values provide counts of the nodal lines: l is the number of nodal lines parallel to the y direction, m the number parallel to the x direction. For example, Fig. 1 shows the

experimenter investigating the nodal line structure for the third normal mode, $p_{1,1}$, with a single vertical and a single horizontal nodal line which intersect at the center of the cavity.

If the ratio of the rectangular cavity boundary lengths is rational, then there will be pairs of distinct normal modes with the same wave number: $k_{l,m} = k_{l',m'}$. Such a pair is then *degenerate*, and linear combinations of them are also eigenfunctions with the same eigenvalue k^2. These linear combinations can have nodal line structures which are very different from those of the original $p_{l,m}$ and $p_{l',m'}$. Our cavity has a design $L_y/L_x = 3/4$, and the actual cavity differs by only 0.2% from this value. Thus, the cavity was designed to have $k_{4,0} = k_{0,3}$, making this pair degenerate. The common resonant frequency of the pair is 4 times that of the $k_{1,0}$ mode, or 4.528 kHz.

The nodal line structures of these two 4.528 kHz modes are shown in Fig. 10. With the source transducer placed in a corner of the cavity and emitting this degenerate mode frequency, both modes should be excited with equal phases and nearly equal amplitudes. This means that the cavity will respond with a linear combination of the two modes. With the transducer in the lower left corner of the cavity, for example, the cavity should respond with the combination $p_{4,0} + p_{0,3}$. The nodal structure of this state, along with its orthogonal counterpart $p_{4,0} - p_{0,3}$, are shown in Fig. 11.

Note the interesting nodal line structures of the sum and difference combinations shown in Fig. 11: Each nodal line meets a boundary at an angle of 45°, either at a corner or paired with another nodal line along a wall. Each of these intersections is a saddle point of the resultant $p(\mathbf{r})$, satisfying the boundary condition Eq. (A6) because $\nabla p(\mathbf{r}) = 0$ at these points. Particularly relevant to the measured cavity frequency response is the observation that diagonally opposite corners of the cavity represent antinode–node pairs. The source will occupy the antinode position, and a diagonally opposite position of the detector will be on a nodal line, causing the frequency response to show a sharp decrease at the degenerate mode frequency. This behavior could not occur at a nondegenerate resonance, where all corners are antinodes of the individual $p_{l,m}$ eigenfunctions, Eq. (A10).

Of course, any real cavity is not a perfect rectangle with a side length ratio of exactly 4:3. Thus, this degeneracy due to an ideally shaped, lossless cavity will be broken by any actual resonant cavity. A real cavity also would not have zero loss; however, so its resonances have nonzero quality factors Q, and this makes all the difference. If the errors in the shape of the cavity break such a degeneracy by a fractional frequency shift smaller than the resonances' nominal $1/Q$, then two nearly degenerate modes may be mixed

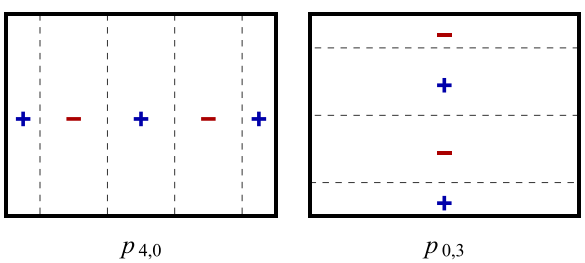

Fig. 10. Nodal line structures of the ($l = 4$, $m = 0$) and ($l = 0$, $m = 3$) degenerate cavity modes. Also shown are the signs of the pressure phasor fields in the areas between nodal lines.

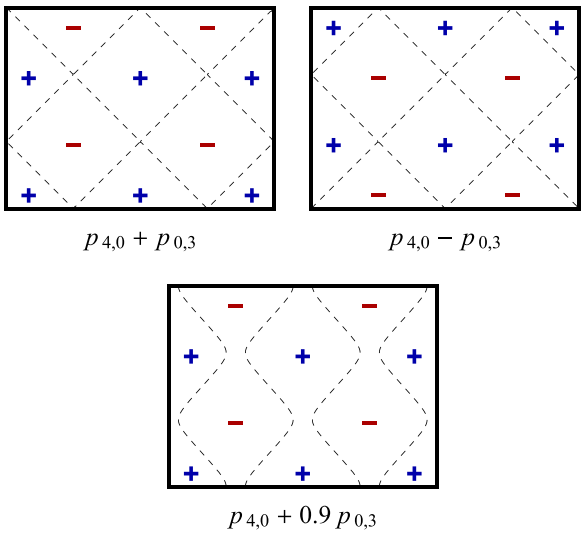

Fig. 11. Nodal line structures of linear combinations of the ($l = 4$, $m = 0$) and ($l = 0$, $m = 3$) degenerate cavity modes. These two linear combinations form an alternative, orthogonal pair of states spanning the subspace of degenerate modes at this frequency. Also shown is an example of a linear combination with unequal amplitudes.

strongly enough to behave in a way that is well-approximated by this ideal description. Such is the case with the cavity of Fig. 1, who response at 4.53 kHz, shown in Fig. 8, exhibits behavior that is consistent with the antinode–node response of the ideal $p_{4,0} + p_{0,3}$ model, as indicated by the sharp dip confirming the near cancellation of the two modes' responses over a very narrow range of frequencies—a behavior present both in the actual data and in the MOI model.

In fact, for the particular design ratio choice of 4:3, there is a further complication involving the $p_{4,0} + p_{0,3}$ degeneracy. The $p_{3,2}$ mode would have a k and frequency which differ from the degenerate pair by only 0.3% at this design ratio. The actual cavity dimensions would assign mode frequencies of

$$(f_{0,3}, f_{4,0}, f_{3,2}) = (4.520, 4.529, 4.541)\,\text{kHz}. \tag{A11}$$

The differences of the successive frequencies are only 0.20% and 0.26%, so with a $Q \approx 150$, these three frequencies form what is effectively a degenerate triplet, complicating the observed frequency response and nodal line structure near 4.53 kHz (cf. Fig. 8).

[a]Electronic mail: rice@caltech.edu, ORCID: 0000-0002-9845-9762.
[b]ORCID: 0000-0003-1529-9423.
[c]ORCID: 0000-0002-5487-1632.

[1]The standard deviation of the observed peak frequencies away from the least-squares fit to $\omega(k) = v_\phi k$ was only 2.1 Hz for frequencies below 3.5 kHz. The phase velocity v_ϕ of sound was determined from the fit to be 344.79 ± 0.24 m/s in excellent agreement with that calculated using an ideal gas expression for dry air at the measured lab temperature of 22.4 C: 344.72 m/s. See, for example, the *HyperPhysics Concepts* website of Georgia State University, *Speed of Sound*: <http://hyperphysics.phy-astr.gsu.edu/hbase/Sound/souspe3.html>.

[2]By "phasor" we mean, not the science fiction weapon, but the signal's complex-valued amplitude and phase at time $t = 0$. We then get the phase at any other time by multiplying the phasor by $\exp(-i\omega t)$. Note that we use the "physics phase convention" for a traveling wave: $\exp(i\,\mathbf{k}\cdot\mathbf{r} - i\omega t)$, rather than the "engineering convention" $\exp(j\omega t - j\,\mathbf{k}\cdot\mathbf{r})$. Of course, i and j each denote $\sqrt{-1}$, but the differing symbols might provide the reader with

a hint as to which convention is being used (and j avoids possible confusion with a symbol for electrical current).

[3]Those "in the know" will recognize this discussion as providing a somewhat simplified version of a wave representation of the signals on the transmission line, where we have taken the line's characteristic wave impedance $\equiv 1$. The current phasor on the line at position x is then $I(x) = V_+(x) - V_-(x)$, and a free boundary for the voltage becomes a fixed boundary for the current, e.g., $I(L) = V_+(L) - V_-(L) = 0$.

[4]Wikipedia describes several of these methods, e.g., <https://en.wikipedia.org/wiki/Finite_element_method>, <https://en.wikipedia.org/wiki/Method_of_moments_(electromagnetics)_>.

[5]In general, the method of images (MOI) enjoys a long history in the computer-aided engineering analysis of room and structural acoustics. Pioneered in a now-classic paper by Allen and Berkley (Ref. 15), it used image sources to estimate the time-domain, reverberation response of a room to a short sound impulse. The resulting reverberation time envelope characterizes the suitability of a space as, for example, a lecture hall or recording studio, a diagnostic introduced in 1895 by W. C. Sabine (Ref. 16). The method does not, however, employ coherent superposition of waves from the source and its reflections, and it is, therefore, unsuitable for frequency response calculations of a cavity whose dimensions are of the order of a wavelength, as in our case. The use of MOI-based calculations of a space's acoustic reverberation response has become a standard of the industry. The Wayverb website, Ref. 17, includes a summary of current techniques employed by several popular acoustic engineering tools: <https://reuk.github.io/wayverb/context.html#existing-software>. All of these tools, however, are inappropriate for the task at hand.

[6]George Green, *An Essay on the Application of Mathematical Analysis to the Theories of Electricity and Magnetism* (T. Wheelhouse, Nottingham, England, 1828). Available at Google Books <https://books.google.com/books?id=GwYXAAAAYAAJ>. Also, definitions and examples are available in: John D. Jackson, *Classical Electrodynamics*, 3rd ed. (John Wiley and Sons, Inc., New York, 1998), ISBN 978-0471309321.

[7]We consider only specular reflections for our model, so that angles of incidence and reflection are equal. The assumed ideal, rigid boundaries have reflection coefficients equal to unity, independent of the angle of incidence. These assumptions are quite accurate for the thick, rigid walls of the small resonant cavity under consideration. For large cavities (such as offices, classrooms, or auditoriums), these assumptions are inadequate, because diffuse reflections and wall losses (attenuation) are nontrivial and can be strongly dependent on the angle of incidence.

[8]The requirement that multiple mirror images of the cavity generated as described completely tile the plane and have disjoint interior regions greatly restricts the geometries of candidate cavities for this method. Rectangles and equilateral triangles are among the very few available. More complicated algorithms can be used to generate the set of image sources for a more general range of polygonal cavity shapes, but such considerations are beyond the scope of this paper. For examples see the quite sophisticated approach presented by Cuenca *et al*., in their 2009 paper, Ref. 18. It employs coherent MOI superposion to analyze the frequency responses of elastic vibrations in thin, convex, solid plates.

[9]Of course, the RHS of Eq. (10) does not evaluate to a pressure amplitude. It should be scaled by a factor representing the pressure phasor amplitude at some standard distance δ from the source, e.g., $p(\delta)\delta^{1/2}$. As will be seen, this factor is unimportant for our analysis, so it may be taken to be $\equiv 1$.

[10]This result leads to a conclusion analogous to the venerable "Olbers paradox" of cosmology (H. R. Olbers, 1823). See, for example, Edward R. Harrison, *Darkness at Night: A Riddle of the Universe* (Harvard U. P., Cambridge, 1987), ISBN 978–0674192706. See also: <https://en.wikipedia.org/wiki/Olbers_paradox>

[11]The algorithm as implemented could perform approximately 1.8×10^6 image $p(r)$ calculations per second of CPU time on a fairly modest desktop: 3.1 GHz, 4-core ®Intel i5 with 16 GB RAM. Two versions of the notebook are provided: `MOIannotated.nb` has heavily commented ®MATHEMATICA code explaining its details and including example function calls, whereas `MOI.nb` is much more terse and streamlined. The website also holds other files related to acoustic cavity resonance investigations. <http://sophphx.caltech.edu/MOI>.

[12]At the "standard" threshold of human hearing, 0 dB SPL (sound pressure level), a sound wave's RMS pressure amplitude is approximately 2×10^{-10} standard atmospheres, or about 0.15 μtorr. At 121 dB SPL, over a million times the threshold amplitude, measured vibration amplitude of the human eardrum in the area where it is coupled to the inner ear is 350 nm; at 0 dB SPL, this would correspond to an amplitude a million times smaller, or only $\sim 1/300$ atomic radius. See: Juergen Tonndorf and Shyam M. Khanna, "Tympanic-membrane vibrations in human cadaver ears studied by time-averaged holography," J. Acous. Soc. Am. **52**, 1221–1233 (1972).

[13]E. A. Dean, "Atmospheric effects on the speed of sound," Technical Report No. AD-A076060, Defense Technical Information Center (1979) <http://sophphx.caltech.edu/MOI/Dean_1979.pdf≥.

[14]Carl Gottfried Neumann (1832–1925), German (Prussian) mathematician. He made several important contributions to applied mathematics and mathematical physics. See the MacTutor History of Mathematics Archive website, <https://mathshistory.st-andrews.ac.uk/Biographies/Neumann_Carl/>.

[15]Jont B. Allen and David A. Berkley, "Image method for efficiently simulating small-room acoustics," J. Acoust. Soc. Am. **65**, 943–950 (1979).

[16]Harvard professor Wallace Clement Sabine (1868–1919) was arguably the "father" of architectural acoutics and its use of *sound reverberation* time as a primary indicator of the suitability of a space's acoustics for concert music or as a lecture hall. Modern computational methods for architectural acoustic design are clearly directly descended from his successful 1895 effort to improve the acoustics of a lecture hall on the Harvard campus. See Wallace Clement Sabine, *Collected Papers on Acoustics* (Harvard U. P., Cambridge, 1922). Available at *Internet Archive's Open Library*: <https://openlibrary.org/works/OL160998W>.

[17]The *Wayverb* website ([copyright] Reuben Thomas, 2016) provides open-source software for acoustic modeling of large rooms and structures. The software, which has not been used or endorsed by the authors, is described as employing a variety of modeling techniques. Available at: <https://reuk.github.io/wayverb/>.

[18]Jacques Cuenca, François Gautier, and Laurent Simon, "The image source method for calculating the vibrations of simply supported convex polygonal plates," J. Sound Vib. **322**, 1048–1069 (2009).

Modeling the frequency response of an acoustic cavity using the method of images

Frank Rice, Teresa Riedel and Isaiah Curtis

Citation: American Journal of Physics **91**, 288 (2023); doi: 10.1119/5.0124415
View online: https://doi.org/10.1119/5.0124415
View Table of Contents: https://aapt.scitation.org/toc/ajp/91/4
Published by the American Association of Physics Teachers